Contents lists available at ScienceDirect

Electrochimica Acta

High-efficiency dye-sensitized solar cells with hierarchical structures titanium dioxide to transfer photogenerated charge

Peilu Zhao [a], Shiting Yao [a], Meng Wang [a], Biao Wang [b], Peng Sun [a], Fengmin Liu [a,*], Xishuang Liang [a], Yanfeng Sun [a], Geyu Lu [a,*]

[a] College of Electronic Science and Engineering, Jilin University, PR China
[b] Changchun Institute of Optics, Fine Mechanics and Physics, PR China

ARTICLE INFO

ABSTRACT

Hierarchical TiO_2 nanorod-sheet-flowers (TNRSFs) consisting of one dimensional (1D) vertically aligned rutile TiO_2 nanorods array (TNRA), 2D TiO_2 nanosheets (TNSs) and 3D TiO_2 nanoflowers (TNFs) have been synthesized via a simple NaOH-assisted hydrothermal method and employed as an photoanode for high-efficiency dye-sensitized solar cells (DSSCs). In our strategy, The TNFs layer with large thickness can potentially enable a great amount of dye adsorption and significantly strengthen the light-harvesting ability, which is beneficial for generating more charge. In addition, The TNRA and TNSs act like charge collectors, providing efficient transport pathways for electrons, which means the photogenerated charge can be collected efficiently through this conducting network. The electrochemical impedance spectroscopy (EIS) measurement shows that the TNRSF film possesses better electron transport ability and longer electron lifetime (28.4 ms) compared with the TiO_2 nanoparticals (TNPs) film. Furthermore, an overall power conversion efficiency of 8.41% (with a J_{sc} of 16.95 mA cm^{-2}, V_{oc} of 0.73 V and FF of 68%) is achieved for the DSSC based on the TNRSF photoanode, indicating a 51.8% enhancement compared with that of the TNPs photoanode (5.54%). The discoveries from this work highlight the significance of designing photoanode materials with hierarchical structures for enhanced photovoltaic performance.

© 2015 Elsevier Ltd. All rights reserved.

1. Introduction

With the strong demand in environment-friendly and renewable energies, solar energy is now attracting global attention. Dye-sensitized solar cells (DSSCs), with advantages of simple fabrication procedures, low manufacturing cost and high theoretical efficiency, have been considered as promising candidates for next-generation solar cells [1],[2], [3] and [4]. During the last two decades, much effort has been devoted to the development of high performance of DSSCs [5], [6], [7], [8] and [9].

In a typical DSSC, light is harvested by dye molecules which are adsorbed by the photoanode materials to generate free electrons. Therefore, light-harvesting efficiency has been one of the key issues affecting the DSSC performance. Compared with designing novel dye sensitizers for absorbing a wider range of light, constructing the photoanodes to improve the amount of dye adsorption and enhance light scattering is relatively simple. Intensive researches have been proposed in order to enhance

the light-harvesting efficiency of DSSCs to date [10], [11], [12], [13] and [14]. As is well known, zero dimensional (0D) TiO_2 nano-particals (TNPs) such as P25 possesses strong dye adsorption ability because of its large specific surface area. However, The electron trap states due to impurity segregation, located at grain boundaries, are likely to be high in TNP films due to poor connectivity of the particles. 1D nanostructure with less such trap states has proven to be an effective way to facilitate electron transfer [15], [16] and [17]. However, the conversion efficiency of nanowire/nanorod-based DSSCs still stays at a relatively low level mainly due to the insufficient surface area for dye adsorption and the lack of light scattering ability. To overcome the dilemma, some strategies have been presented. For example, Joshi et al. reported that a composite made of electrospun TiO_2 nanofibers and conventional TNPs could enhance electron transport and light scattering with slight dye uptake reduction, demonstrating higher device efficiency than those made of TNPs alone [18] and [19]. Meanwhile, many researchers have worked on enhancing the surface roughness and improving the length of nanorods to increase the dye uptake. In our strategy, designing hierarchical TiO_2 photoanode nanomaterials with a light-scattering layer on the top of the electron transport layer can be widely adopted as it will

* Corresponding authors.
  E-mail address: lugy@jlu.edu.cn (G. Lu).

improve the photogenerated charge-transfer efficiency dramatically and thereby enhance the photocurrent density [20] and [21]. Although some scattering materials with high specific surface areas can provide dual-function of offering both light-scattering and large dye adsorption, they still suffer from longer electron transit time and lower effective diffusion coefficients due to the poor electrical contact between nanocrystallite domains [22] and [23].

In this work, we firstly developed a one-step hydrothermal method to directly synthesize 3D TiO$_2$ nanorod-flowers (TNRFs) film which was composed of 1D TiO$_2$ nanorods array (TNRA) and 3D TiO$_2$ nanoflowers (TNFs). This kind of material with unique nanostructure was applied to photoanode for DSSCs which obtained a higher photocurrent density, leading to an enhanced PCE of (6.83%) than P25 (5.54%). This is primarily attributed to the strong light-scattering ability and sufficient dye uptake of the TNFs layer. We further successfully synthesized the hierarchical TiO$_2$ nanorod-sheet-flowers (TNRSFs) based on the TNRF by using a NaOH-assisted hydrothermal method. The existence of 2D TiO$_2$ nanosheets (TNSs) can promote the electron transmit process, since TNSs establish good electrical contact between TNRA and TNFs layer, and also have tight connection with surrounding TNFs. The UV–vis reflectivity spectra indicate that the TNRSF film has higher reflectivity in the wavelength range of 400–800 nm than TNRFs film, and the UV–vis absorption spectra of the dye desorption solutions also show that the TNRSF film has excellent dye adsorption capacity. Moreover, the EIS study provides more detailed information about photoelectric properties of the cell constructed using TNRSF, demonstrating high charge-transfer efficiency and long electron lifetime. Finally, the TNRSF based cell obtains a PCE of 8.41%, exhibiting an improvement of 23.1% and 51.8% compared with cells based on TNRF and absolute TNPs film, respectively.

2. Experiments

2.1. Synthesis of the materials

All starting chemicals were analytical grade and used without further purification. The synthetic process of the 3D TNRF and hierarchical TNRSF is shown in Fig. 1, which consists of two steps,
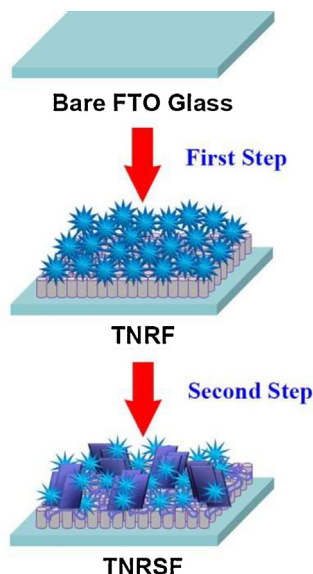

Fig. 1. Schematic illustration of the fabrication process of the hierarchical 3D TNRSF via two steps of hydrothermal reaction.

and the second step applies a NaOH-assisted route to synthesize the TNRSF. In brief, 4 mL HCl (36 wt.%) was added to 6 mL deionized water with vigorous stirring, then X mL Tetrabutyl titanate (TBT) was added into the mixed solution and stirred until form a transparent solution. The mixture was transferred into a 45 mL Teflon-lined autoclave. A piece of F-doped SnO$_2$ (FTO) glass (resistivity 14 Ω /square, Nippon Sheet Glass, Japan) ultrasonically cleaned in acetone and deionized water for 30 min, respectively, was placed in the autoclave which was then sealed and heated at 180 °C for 3 h. After the autoclave cooled to room temperature, the TiO$_2$ film grown on the FTO was washed several times with distilled water and dried in an oven at 80 °C for 6 h. To investigate the dosage of precursor TBT on the morphology and property of the product, the X value was set to 0.2, 0.3 and 0.4, while the corresponding products were denoted as TNRF-2, TNRF-3 and TNRF-4, respectively. Finally, the TNRF-X samples were calcined at 500 °C for 1 h with a heating rate of 2 °C min^{-1} in air. The TNRF-3 was selected for the next step due to its great photoelectric properties based on our previous test. The second step: generating of the nanosheets, according to our previous experience [24], we applied a simple strategy to directly convert the 3D TNRF into a novel hierarchical structure to further improve the light-harvesting efficiency and electron transport property of the film. The TNRF-3 film was placed at the bottom of the Teflon-lined which contained 30 mL of 10 M NaOH solution with the nanorods side facing up, and maintained at 180 °C for 4 h, then allowed to cool to room temperature naturally. The as-prepared sample was washed with distilled water thoroughly, and the TNRSF film was obtained by exchanging alkaline ions in sodium titanate with protons from a dilute HNO$_3$ aqueous solution, following a heat treatment in a muffle furnace at 500 °C for 1 h.

2.2. Fabrication of the DSSCs

To prepare a screen-printable P25 paste, 0.6 g of P25 powder was dispersed in the mixture of 10 mL of ethyl alcohol and 2 g of α- terpineol and treated with an ultrasonic bath for 60 min to form a slurry, then 1 g of ethyl cellulose and 6 g of ethyl alcohol were added to the slurry with continuous stirring for 24 h to obtain viscous white paste. The P25 paste was coated on the clean FTO glass using the doctor blade technique. After drying at 120 °C for 15 min, the P25 film was subsequently annealed at 450 °C for 30 min in air. Then the five films were immersed in a 40 mM TiCl$_4$ aqueous solution at 70 °C for 30 min before being sintered at 500 °C for 30 min. After cooling down to 80 °C, the films were loaded with dye by immersing it in a 0.4 mM dye solution (dye: N-719, solvent: t-butanol and acet-onitrile mixture with volume ratio of 1:1) for 24 h at room temperature. Finally, the dye-sensitized films were sandwiched together with the Pt-coated FTO counter electrode. The acetonitrile/valeronitrile (v/v, 85/15) electrolyte containing 0.6 M 1,2-dimethyl-3-propylimidazolium iodide, 0.03 M I$_2$, 0.1 M guanidinium thiocyanate and 0.5 M 4-tertbut-ylpyridine (Aldrich) was injected into the space between the anode and the cathode by using a vacuum back-filled method.

2.3. Measurements of DSSCs' performance

The crystal structure of the as-synthesised sample was investigated by X-ray diff ; ;raction (XRD; Rigaku TTRIII, with Cu Kα1 radiation). A filed-emission scanning electron microscopy (FESEM, JEOL JSM-7500F, operated at an acceleration voltage of 15 kV) and a transmission electron microscopy (TEM, JEOL EM-2100, using an acceleration voltage of 200 V) were employed to characterize the morphological and structural properties of all the samples.
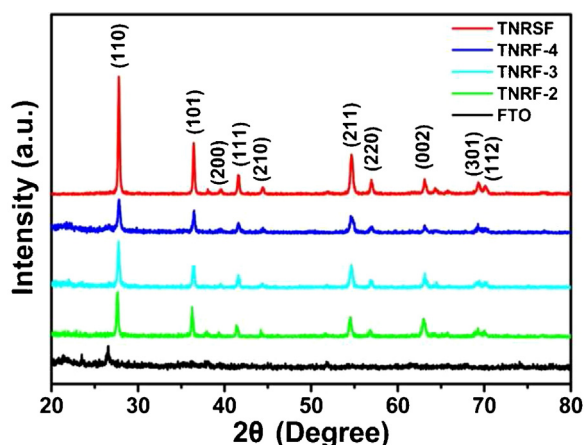
Fig. 2. XRD patterns of the four kinds of TiO₂ film photoanode and a FTO glass substrate.

The current–voltage (I–V) characteristics of the solar cells were measured using Keithley 2400 Source Meter under illumination (AM 1.5G, 100 mW cm^{-2}) with a solar light simulator (Newport, model: 94023A) which was calibrated with a NREL-calibrated silicon solar cell equipped with an optical filter. Diffuse-reflectance spectra of the samples and UV–vis absorption spectra of desorption dye from different anodes were performed on a Perkin-Elmer UV–vis spectrophotometer (SHIMADZU 2550). The incident photon-to-current efficiency (IPCE) spectra were measured as a function of wavelength from 400 to 800 nm with a spectral resolution of 5 nm on the basis of a Spectral Product Zolix DSC300PA. Electrochemical impedance spectroscopy (EIS) was recorded using an electrochemical workstation (Solartron SI1287). The frequency range was varied from 0.1 Hz to 10^6 Hz, and the applied bias voltage was set to the open-circuit voltage (V_{oc}) of the DSSCs.

3. Results and discussion

3.1. Characterization of materials

The three samples prepared in different precursor concentration (TNRF-X: TNRF-2, TNRF-3, TNRF-4) and TNRSF were initially examined by XRD measurement. Fig. 2 shows that except for diffraction peaks arising from FTO glasses, the well-defined and sharp Bragg peaks with high intensities indicate the good crystallinity of the four samples. As can be seen from the XRD patterns, the 2θ values at 27.44, 36.04, 39.28, 41.36, 44.16, 54.40, 56.52, 62.77, 69.02 and 69.90 can be indexed to distinct rutile TiO₂ (JCPDS no. 21-1276). The TNRSF shows the stronger diffraction peaks such as (1 0 1), (1 1 1), (2 1 1), (2 2 0) and the most prominent diffraction peak (1 1 0), indicating the improved crystallinity, which is beneficial for electron transport.

SEM observations on the surface and the cross-sectional morphology of the three TNRF-X samples have been initially made. Fig. 3 (a-f) successively shows typical SEM images of the hierarchical films obtained from different reaction solutions (the added TBT volume is 0.2, 0.3, 0.4 mL). Fig. 3(a, b and c) display the cross-sectional images of TNRF-2, TNRF-3 and TNRF-4, respectively, indicating that the hierarchical films consist of vertically aligned 1D nanorods and 3D nanoflowers. As can be seen from the cross-sectional images, the TiO₂ nanorods of the three films have nearly the same length (~3.7 μm), implying that when the introduced TBT increases to 0.2 mL, redundant precursor had no promotion effect on the growth of the TNRA. The thicknesses of TNF layer are almost the same (average thickness = 22.8 μm), which guarantees the same adsorption area for dye molecules. Top-view SEM images of the produced three films are shown in Fig. 3(d, e and f). The inset in each image provides a higher magnification of a representative TNF which consists of numerous nanorods. This TNFs layer has good porosity and connectivity, which can increase the dye uptake and electron transport property. With the increasement of TBT addition, the resultant TNFs become plumper, and tend to be spherical structure (inset of Fig. 3(f)). Moreover, it is noteworthy that the nanorods become agglomerate in the center of TNFs (Fig. 3(c)), which is different from that of TNRF-2 and TNRF-3. Above results indicate that the concentration of TBT is highly associated with the hydrothermal growth of TNRFs.

TEM images of a representative nanorod broken from the TNF are presented in Fig. 4. Inset (a) provides the further information about the interior structure of an intact nanoflower, implying the poor porosity inside of it. But the rough surface composed of tiny rutile TiO₂ nanorods still show the porous nature of TNF. The HRTEM image (Inset (b)) clearly shows that the interplanar spacing of ~ 0.30 nm and ~ 0.32 nm of the nanorod correspond to the (0 0 1) and (1 1 0) lattice planes of rutile TiO₂ phase, by which
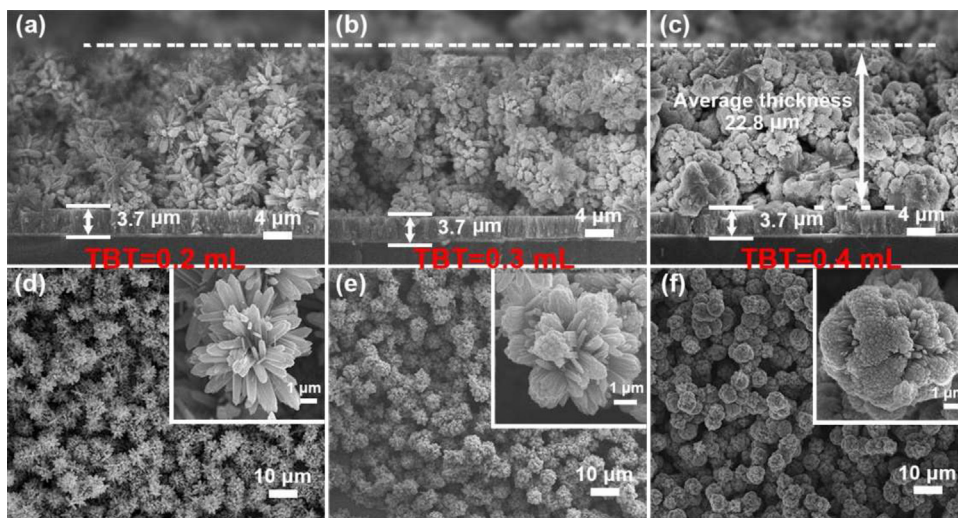

Fig. 3. SEM images of three kinds of TNRF film synthesized by hydrothermal treatment with different amounts of Ti-precursor. (a-d) 0.2 mL, (b-e) 0.3 mL and (c-f) 0.4 mL. (a, b and c) cross-section and (d, e, f) top view.
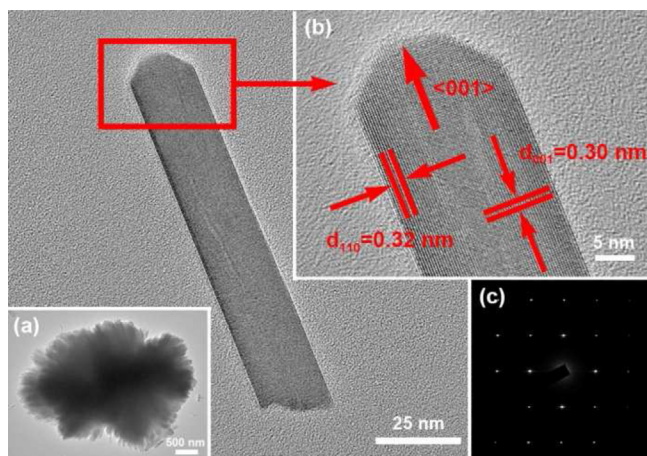
Fig. 4. TEM images of a representative nanorod broken from the TNF, inset (a) a single TNF from TNRF-4, (b) HRTEM image and (c) SAED pattern of the nanorod.

the nanorod can be identified to grow along $\langle 0\,0\,1 \rangle$ direction. Inset (c) is the SAED pattern, revealing a monocrystal rutile phase of the TiO_2 nanorod. Fig. 5(d) shows SEM images (cross-section) of the synthesized TNRSF film, and Fig. 5 (h) are the corresponding top view. Fig. 5(d) and (h) indicate that numerous 2D TNSs with diameters in the range of 10–30 μm and length up to $\sim$ 16.7 μm cover the substrate, and look like leaves interlacing each other. The newly synthesized TNSs which grow throughout the TNFs layer show tight connection with both of the TNRA and TNFs, resulting in more efficient charge collection and faster electron transport. The magnified SEM images shown in inset of Fig. 5(h) indicate that the TNFs become smaller compared with that of TNRF-3, which is mainly ascribed to the corrosion effect caused by NaOH solution. In order to understand better about the growth process of TNRSF, we also provide a series of SEM images of the products at different reaction times. Fig. 5(a-c) shows that the diameter of TNSs increases dramatically when the synthetic process is extended, while the thickness of TNFs layer decreases from $\sim$20 μm to $\sim$13 μm, which is mostly attributed to the conversion process from 3D TNFs into 2D TNSs (Fig. 6(c)). It is interesting to note that the TNSs start to form on the surface of TNRA, and finally grow throughout the TNFs layer. It can also be observed that the quantity of TNSs increases with the extended reaction time (Fig. 5(e-g)), and numerous TNSs have been formed among the TNFs after 3.5 h.

3.2. Growth process and mechanism

The formation mechanism of 3D TNRF is a typical deposition process (Fig. S1, ESI). It is noticed that both of the average diameter of TNFs and the thickness of TNFs layer deposited on the TNRA increase as the reaction time prolongs. Furthermore, the volume of the reaction solution plays a crucial role in the deposition of TNFs. Experiments show that increasing the volume of the reaction solution without changing the ratio of the components will make it difficult for the TNFs to deposit on the surface of TNRA. This may be ascribed to the increased filling content of autoclave which improves the relatively pressure and inhibits the deposition process. Based on the above results, schematic diagram is presented to illustrate the possible growth process of the TNRF film (Scheme S1, ESI).

To reveal the formation process and the possible growth mechanism of the TNRSF, the partial magnified SEM images are presented in Fig. 6. There exit some nanomesh between the nanorods, mainly due to the surface corrosion of individual nanorod by NaOH (Fig. 6(b and c)), and this porous structure is beneficial for adsorbing more dye molecules [25]. Since the corrosion rates of the various crystal faces are different, and extension of the reaction time causes further agglomeration of the nanomesh, the hierarchical 2D nanosheet structure is formed through an oriented attachment process (Fig. 6(a and b)). This reaction can be described as follows.

$$TiO_x + NaOH \rightarrow Na_2TiO_3 + H_2O$$
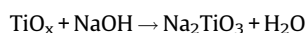
The Na–O–Ti links on the surface of the products are believed to react with acid and water to form new H–O–Ti and Ti–O–Ti links [26]. After annealing at 500 °C for 1 h, the pure TiO_2 with no other components is obtained (Fig. S2, ESI). On the basis of above observations (Fig. 5, 6), we are apt to describe the crystal growth mechanism of the nanosheet structure as involving a sequence of dissolution, recrystallization and agglomeration, leading to the evolution of nanosheet morphology. The schematic diagram of the TNRSF crystal growth is displayed in Scheme 1.

3.3. Photovoltaic performance

To determine the effect of this 3D TiO_2 assembly on the photovoltaic properties of DSSCs, we fabricated cells with P25, TNRF-2, TNRF-3, TNRF-4 and TNRSF films as photoanodes. After dye loading, the photocurrent density voltage (J-V) curves under AM 1.5 (100 mW cm^{-2}) illumination with an active area of 0.25 cm^2
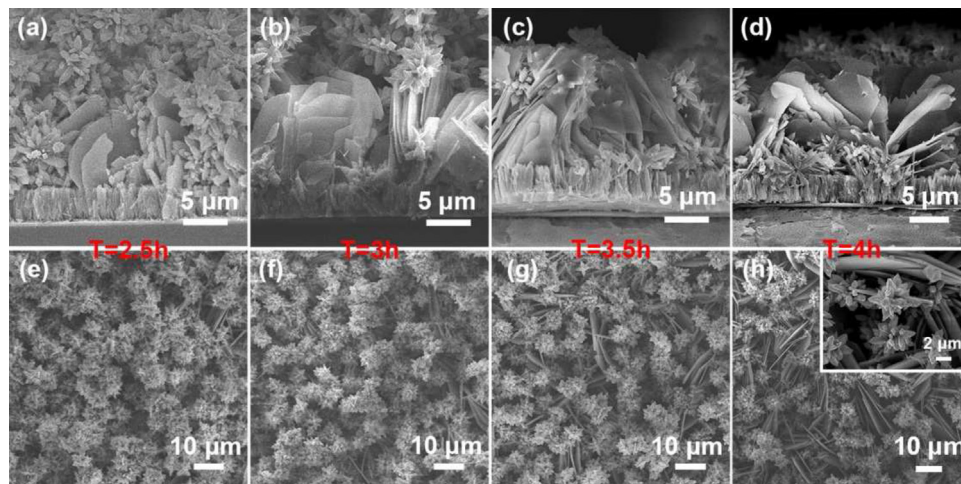

Fig. 5. SEM images of TNRSF at different reaction times, (a, e) 2.5 h, (b, f) 3 h, (c, g) 3.5 h and (d, h) 4 h. (a-d) cross-section and (e-h) top view.
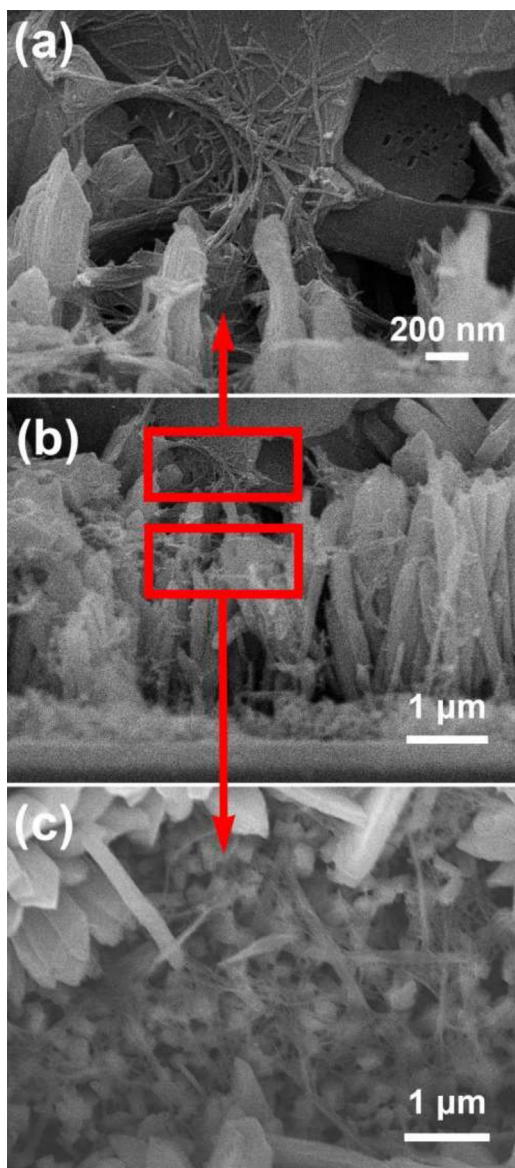
Fig. 6. Magnified SEM images of (a) nanosheet, (b) TNRSF film (cross-section) and (c) nanomesh in the TNRA (top view).

were measured and presented in Fig. 7(a). The corresponding photovoltaic parameters are summarized in Table 1. The DSSC made with P25 achieves a short-circuit current density (J_{sc}) of 13.56 mA cm^{-2}, the smallest fill factor (FF) of 55 % and an energy conversion efficiency (η) of 5.54 %. Among these TNRF-X based
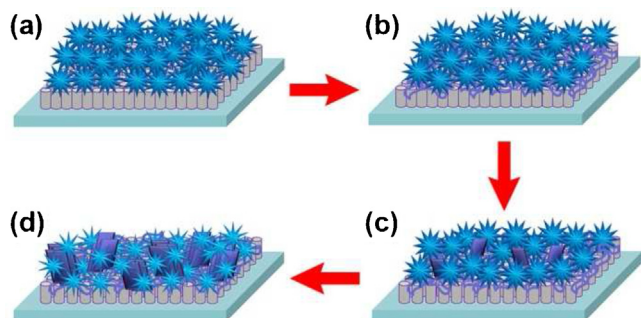
cells, the cell assembled with TNRF-3 demonstrates the highest J_{sc} of 14.73 mA cm^{-2} and η of 6.83%, 23% improvement over the P25 based cell. It is noteworthy that after the hydrothermal treatment, the cell based on the resultant TNRSF film enhances photoelectric properties drastically, which exhibits a J_{sc} of 16.95 mA cm^{-2}, V_{oc} of 0.73 V, FF of 68%, and thus a higher η up to 8.41%. The TNRSF photoanode achieves the best performance among the five cells, mainly resulting from the increase of J_{sc} and FF. Three primary reasons contribute to the increasement: (i) the improved dye adsorption by the introduced TNFs and TNSs, (ii) the enhanced light harvesting efficiency due to the strong light scattering effect of TNFs layer (Fig. 7(b)), and (iii) the more efficient electron transfer pathway provided by TNSs, which plays a vital role for high-efficiency energy conversion.

The large amount of dye adsorption and enhanced light scattering effect are considered to be two main factors influencing light-harvesting efficiency and hence incident photon to current efficiency (IPCE) of the resulting DSSC. Measured diffuse reflectance and absorption spectra of the five un-dyed and dyed bare electrode films are displayed in Fig. 8. The P25 film exhibits a diminishing scattering effect in the visible light wavelength region (400–800 nm), whereas the TNRF-X films shows much stronger reflectance. We ascribe this to the appearance of 3D TNFs with rough surface which can be likely to lead a strong scattering effect. It is noteworthy that the TNRF-4 has a better light-scattering ability than TNRF-2, which is because its novel surface structure consisting of many small TiO$_2$ nanorods can provide much more scattering centers and longer light travelling distance, thus the solar cell can harvest much more incident light. While the TNRF-2 composed of sparse TiO$_2$ nanorods leads to the apparently weaker scattering effect, some incident light is lost. So the stronger light-harvesting ability of TNRF-4 than TNRF-2 is reasonable (Fig. 8 (b)). As shown in Fig. 7(b), the incident light is significantly
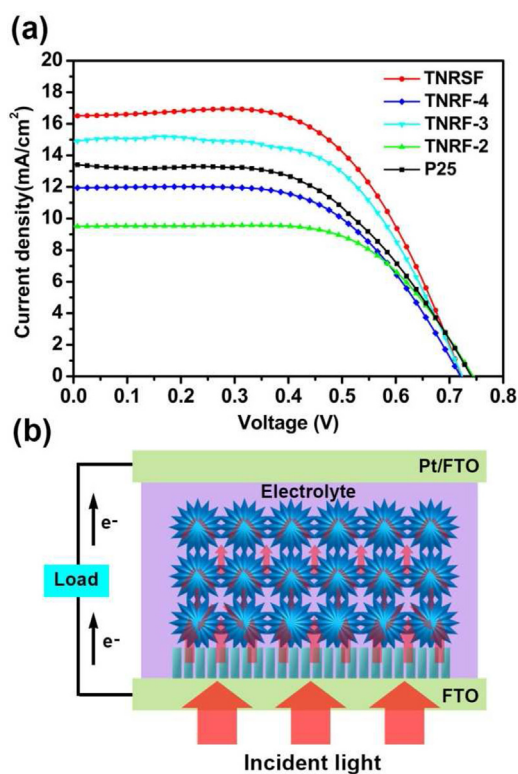

Scheme 1. Schematic diagram of the 3D TNRSF nanostructure growth mechanism.

Fig. 7. (a) J–V curves for cells based on the five photoanodes. (b) Schematic illustration of multiple light reflection and scattering favoured by TNFs layer and the construction of a typical TNRF-X based cell.

Table 1
Average photovoltaic data of five different photoanodes, measured under one sun illumination (AM 1.5 G 100 mW cm^{-2}) and simulative value of resistance (R_1, R_2, and R_3) from EIS spectra calculated by equivalent circuit as shown in Fig. 11.

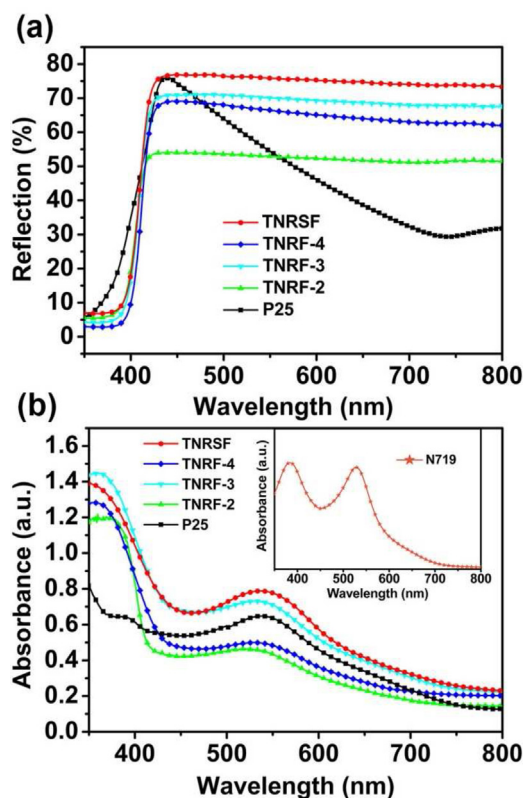| DSSCs	J_{sc} (mA cm^{-2})	V_{oc} (V)	FF (%)	η (%)	$R_1(\Omega)$	$R_2(\Omega)$	$R_3(\Omega)$	dye adsorbed ($\times 10^{-7}$ mol cm^{-2})
P25	13.56	0.74	55	5.54	25.7	8.6	30.6	1.64
TNRF-2	9.59	0.75	66	4.69	23.3	7.1	20.1	1.09
TNRF-3	14.73	0.73	64	6.83	35.5	5.9	22.9	1.48
TNRF-4	11.89	0.72	60	5.19	30.6	9.3	24.7	0.94
TNRSF	16.95	0.73	68	8.41	31.2	5.2	18.8	1.55

Fig. 8. (a) Diffuse reflectance spectra of the electrode films before the dye uptaking process. (b) UV–Vis absorption spectra of the electrode films loaded dye.

scattered by the TNFs thereby extending the light path within the electrodes, thus promoting the probability for interaction with the dye molecules in the TNRF-X films. The higher refractive index of rutile TiO$_2$ (2.75) than the anatase counterpart (2.52) also contributes to an enhanced light reflectance. Furthermore, TNRSF exhibits the best li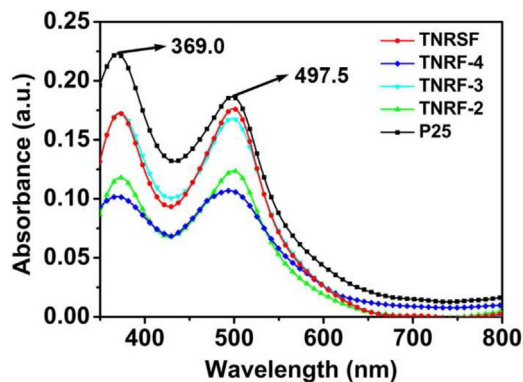ght-scattering capability within the same wavelength range, mostly resulting from the additional effect of TNSs. Fig. 8(b) presents UV–vis absorption spectra of the photoanode films after the dye uptaking process. It is interesting to note that although the P25 film has a weak scattering effect, it still gives a relatively high absorbance performance in the wavelength range of 400 to 700 nm due to its sufficient dye adsorption. On the contrary, the TNRF-2 film shows the weakest light absorption, which is mainly ascribed to its low dye adsorption and poor light-scattering capability. As expected, the TNRSF film exhibits the strongest absorption, implying an effective utilization rate of the incident light.

The UV–Vis absorption spectra of the solutions obtained by thorough desorption in 1 mM NaOH solution were measured in order to further investigate the dye adsorption ability of the five films (Fig. 9). The absorption peaks of UV–Vis spectra arelocated at 369.0 nm and 497.5 nm, which are not exactly in accord with that of Dye N719 (382 nm, 522 nm). This offset is mainly ascribed to the effect on Dye N719 caused by NaOH aqueous solution. According to the Lambert–Beer law, the absorbance is proportional to the solution concentration [27]. The calculated molar quantities of N719 adsorbed on different TiO$_2$ anodes are shown in Table 1. On the one hand, the P25 film shows the highest dye absorption due to its relatively large specific surface area. On the other hand, the dye uptake of the TNRSF film is increased by 4.7% from 1.48×10^{-7} to 1.55×10^{-7} mol cm^{-2} compared to the TNRF-3 film, which is consistent with the analysis that the nanomesh among the TNRA will enhance the dye adsorption amount (Fig. 6(a)). It is interesting to note that the amount of dye adsorbed on the TNRF-4 film shows a 13.8 % and a 36.5% decrease compared with the TNRF-2 film and the TNRF-3 film, respectively. This may be ascribed to that the agglomeration structure in the center of nanoflowers inhibits the TNRF-4 film from adsorbing more dye molecules (Fig. 3(c)).

To analyze the cell performance in more detail, the incident photon-to-current conversion efficiency (IPCE) was measured as a function of wavelength from 400 nm to 800 nm under monochromatic illumination. As shown in Fig. 10, the maxima of the IPCE spectra for all of the DSSCs appear at 525 nm (the peak of the N719 adsorption spectrum). The IPCE of cell TNRF-2 is found to be
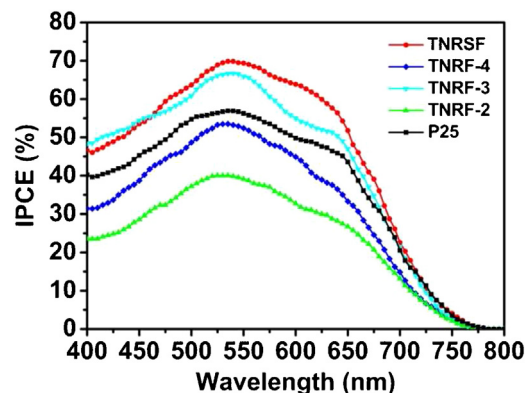

Fig. 9. UV–Vis absorption spectra of desorption dye from five different photoanodes.

Fig. 10. IPCE spectra of the five DSSCs with P25, TNRF-2, TNRF-3, TNRF-4 and TNRSF photoanodes.

the lowest, which is in good accordance with the J–V measurement and dye uptake. Although the TNRF-4 film shows the lowest dye adsorption among the five cells tested, the IPCE still increases by 35% compared to TNRF-2 at around 525 nm, which can be attributed to the stronger light-scattering ability, enabling the more efficient light utilization. The IPCE of TNRSF based cell is the highest one over the almost whole visible region (475-800 nm). Two main characteristics contribute to the IPCE enhancement. First, the sufficient dye adsorption amount and superior light-scattering ability improve the light harvesting efficiency [28] and [29]. Second, the TNSs provide fast electron transport pathways, which facilitate the collection of photoelectrons [30].

In DSSCs, the injected electron concentration and the electron mobility of the photoanode materials have direct effect on the electron transport efficiency. For example, the mobility of bulk TiO_2 is about two orders higher than that of nanocrystalline TiO_2 [31]. As a consequence, new nanostructure of TiO_2 which can facilitate diffusion is particularly significant for electron transport. Electrochemical impedance spectroscopy (EIS) analysis was used to investigate the electron transport and recombination process at the interface in DSSCs. Measurements were taken under the illumination of one sun (AM 1.5 G, 100 mW cm^{-2}) at the open circuit voltage of the cells, and the frequency range was from 0.1 Hz to 10^6 Hz [32], [33] and [34]. Fig. 11(a) and (b) show the Nyquist plots and the Bode curves of DSSCs assembled with five different photoanodes, respectively. The inset of Fig. 11(a) illustrates the equivalent circuit simulated to fit the impedance spectra. Furthermore, the specific impedance data of the DSSCs were analyzed by Z-view software and summarized in Table 1. As can be seen from Fig. 11(a), Nyquist plots of all the cells demonstrate two well-defined semicircles. The larger semicircle at intermediate frequency is attributed to charge transfer resistance at the TiO_2–

dye–electrolyte interface (R_3) [35] and [36], which is vital for the photovoltaic performance. The smaller semicircle at high frequency is attributed to charge transfer resistance at the electrolyte–Pt–FTO interface (R_2). R_1 represents the lumped series resistance for the transport in FTO and all the corresponding resistances outside of the cell. It is noteworthy that the R_3 values of TNRF-X and TNRSF electrodes are significantly smaller than that of P25 film, reflecting that the new 3D assembly accelerates the electron transfer process in the electrode. Moreover, the TNRSF based cell exhibits the smallest R_3, which provides a hint that the electron trapping is minimized in TNRSF film perhaps due to the tight connection of TNFs offered by TNSs, resulting in enhanced electron transport at grain boundaries (interfaces).

The Bode-phase plots (Fig. 11(b)) show a corresponding characteristic frequency peak. Based on the maximum frequency (f_{max}) of the peak at intermediate frequency, the electron lifetime (τ_e) for these five DSSCs can be calculated according to the following equation.

$$\tau_e = \frac{1}{2\pi f_{max}}$$

As observed in Fig. 11(b), the f_{max} values for the cells based on TNRSF, TNRF-4, TNRF-3, TNRF-2 and P25 photoanodes with similar thickness are 5.6, 10.3, 8.1, 7.5 and 11.2 Hz, respectively, and the τ_e of them are calculated to be 28.4, 15.5, 19.6, 21.2 and 14.2 ms accordingly. The much longer τ_e in the cell based on TNRSF photoanode suggests the effective inhibition of electron recombination during the electrons transfer across photoanode films, which means that electrons can transfer a longer distance to a larger extent with unblocked ways across the TiO_2–dye–electrolyte interface, leading to more effective capture and collection of electrons and also confirming the function of TNSs.

As reported previously, the random electrons walking among disordered stacking TiO_2 NPs and 1D electron diffusion along nanorods are two different modes of electron transport in photoanodes, and it is usually believed that the second mode is more facile than within a random NP network because electrons in nanorods do not have to cross many particle boundaries where surface states (electron traps) are mainly located [37] and [38]. This is consistent with the results that P25 based cell shows larger R_3 (30.6 Ω), smaller FF (55%) and shorter τ_e (14.2 ms). Furthermore, the TNRSF based cell exhibits improved electron transport properties compared with TNRF-3 based cell. To further demonstrate possible reasons for significant differences in the electron transport patterns in TNRSF and TNRF-3 films, a simple qualitative model was built (Fig. 12). Compared with TNRSF film, the TNRF-3 film has longer electron transfer pathways, and the transport process is hindered due to the relatively poor connectivity of TNFs (Fig. 12(a)), resulting in shorter τ_e (19.6 ms). In TNRSF
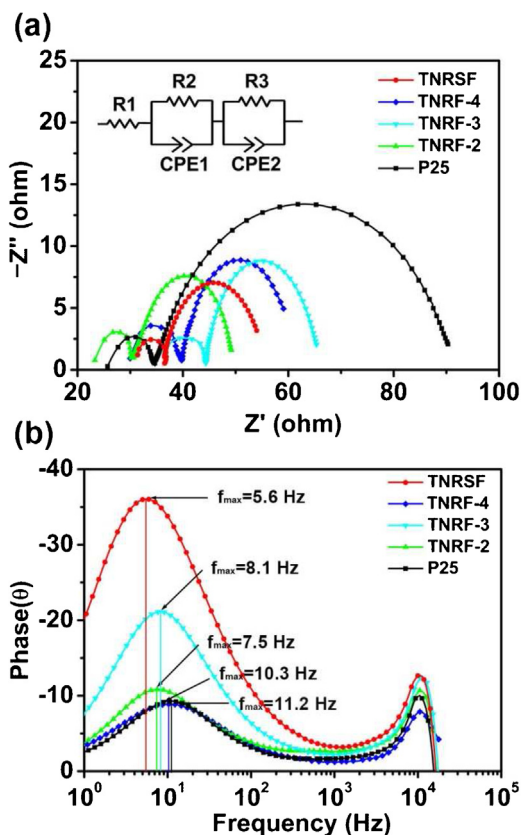

Fig. 11. (a) Nyquist plots and (b) Bode plots of EIS for DSSCs based on photoanodes of P25, TNRF-2, TNRF-3, TNRF-4 and TNRSF.
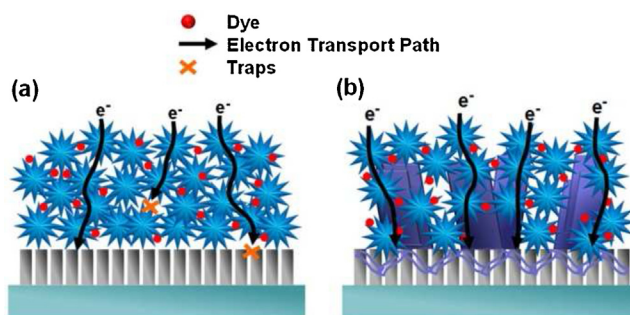

Fig. 12. Simple schematic representations of electron transport patterns in (a) TNRF-X films and (b) TNRSF film.

film (Fig. 5), TNSs act like the charge-collect units, which have tightly interlacement with adjacent TNFs. This novel structure can provide the most efficient electron transfer pathway, and lessen the frequency of electron trapping incidents, which leads to the photoelectrical conversion with the least electrons loss. As a result, longer τ_e (28.4 ms) and higher J_{sc} (16.95 mA cm^{-2}) are observed. The TNRSF also shows enhanced rutile phase, and such high-purity crystallites will contribute to improved electron transport properties [39].

4. Conclusions

In summary, we have successfully synthesized a novel 3D TNRF nanostructure using a surfactant free one-step hydrothermal method, and further prepared hierarchical TNRSF with NaOH-assisted route. Five types of dye-sensitized solar cells (DSSCs) were constructed using TNRF-2, TNRF-3, TNRF-4, TNRSF and P25, respectively. The cell based on TNRF-3 shows a superior short-circuit photocurrent density of 14.73 mA cm^{-2} among the three TNRF-X based cells, and increases by 8.6% compared with that based on P25 film (13.56 mA cm^{-2}), which can be mainly ascribed to higher charge transport rate and sufficient dye adsorption. Among the five cells tested, TNRSF based cell exhibits the highest PCE of 8.41%, indicating a 23.1% and a 51.8% increasement compared with the cells based on TNRF-3 (6.83%) and P25 (5.54%), respectively. Furthermore, the electron lifetime of the TNRSF photoanode achieves a significant improvement from 14.2 ms to 28.4 ms, resulting from the excellent charge-transfer efficiency. These remarkable enhancements of the photovoltaic performance for the TNRSF based cell are mainly attributed to the superior light harvesting, high electron transport rate and sufficient dye adsorption. Hence, we consider that this facile synthesized route will have good potential for application in DSSCs.

Acknowledgements

Appendix A. Supplementary data

Supplementary data associated with this article can be found, in the online version, at http://dx.doi.org/10.1016/j.electacta.2015.04.102.

References

[1] A. Hagfeldt, G. Boschloo, L.C. Sun, L. Kloo, H. Pettersson, Chem. Rev. 110 (2010) 6595.
[2] A. Yella, H.W. Lee, H.N. Tsao, C.Y. Yi, A.K. Chandiran, M.K. Nazeeruddin, E.W.G. Diau, C.Y. Yeh, S.M. Zakeeruddin, M. Grätzel, Science 334 (2011) 629.
[3] B. Oregan, M. Grätzel, Nature 353 (1991) 737.
[4] H.J. Koo, Y.J. Kim, Y.H. Lee, W.I. Lee, K. Kim, N.G. Park, Adv. Mater. 20 (2008) 195.
[5] Y.P. Liu, S.R. Wang, Z.Q. Shan, X.G. Li, J.H. Tian, Y.M. Mei, H.M. Ma, K.L. Zhu, Electrochim. Acta 60 (2012) 422.
[6] N.G. Park, J. van de Lagemaat, A.J. Frank, J. Phys. Chem. B 104 (2000) 8989.
[7] J.Y. Liao, J.W. He, H. Xu, D.B. Kuang, C.Y. Su, J. Mater. Chem. 22 (2012) 7910.
[8] J.G. Yu, J.J. Fan, L. Zhao, Electrochim. Acta 55 (2010) 597.
[9] Q.L. Huang, G. Zhou, L. Fang, L.P. Hu, Z.S. Wang, Energy Environ. Sci. 4 (2011) 2145.
[10] W.Q. Wu, J.Y. Liao, H.Y. Chen, X.Y. Yu, C.Y. Su, D.B. Kuang, J. Mater. Chem. 22 (2012) 18057.
[11] J.Y. Liao, B.X. Lei, H.Y. Chen, D.B. Kuang, C.Y. Su, Energy Environ. Sci. 5 (2012) 5750.
[12] X.H. Tan, P.F. Qiang, D.D. Zhang, X. Cai, S.Z. Tan, P.Y. Liu, W.J. Mai, CrystEngComm 16 (2014) 1020.
[13] H. Pan, J.S. Qian, Y.M. Cui, H.X. Xie, X.F. Zhou, J. Mater. Chem. 22 (2012) 6002.
[14] Q. Zhang, G. Cao, Nano Today 6 (2011) 91.
[15] M. McCune, W. Zhang, Y. Deng, Nano Lett. 12 (2012) 3656.
[16] M. Yang, S. Neupane, X. Wang, J. He, W. Li, N. Pala, ACS Appl. Mater. Interfaces 5 (2013) 9809.
[17] P. Joshi, L.F. Zhang, D. Davoux, Z.T. Zhu, D. Galipeau, H. Fong, Q.Q. Qiao, Energy Environ. Sci. 3 (2010) 1507.
[18] X.X. Wang, S. Karanjit, L.F. Zhang, H. Fong, Q.Q. Qiao, Z. Zhu, Appl. Phys. Lett. 98 (2011) 082114.
[19] S. Hore, C. Vetter, R. Kern, H. Smit, A. Hinsch, Sol. Energy Mater. Sol. Cells 90 (2006) 1176.
[20] T.Y. Tsai, S.Y. Lu, Electrochem. Commun. 11 (2009) 2180.
[21] Z.H. Liu, X.J. Su, G.L. Hou, S. Bi, Z. Xiao, H.P. Jia, Materials Letters 89 (2012) 309.
[22] Z.H. Liu, X.J. Su, G.L. Hou, S. Bi, H.P. Jia, Z. Xiao, Materials Letters 98 (2013) 30.
[23] X.H. Tan, P.F. Qiang, D.D. Zhang, X. Cai, S.Z. Tan, P.Y. Liu, W.J. Mai, CrystEngComm 16 (2014) 1020.
[24] P.F. Cheng, Y. Liu, P. Sun, S.S. Du, Y.X. Cai, F.M. Liu, J. Zheng, G.Y. Lu, Journal of Power Sources 268 (2014) 19.
[25] F. Shao, J. Sun, L. Gao, S.W. Yang, J.Q. Luo, J. Mater. Chem. 22 (2012) 6824.
[26] T. Kasuga, M. Hiramatsu, A. Hoson, T. Sekino, K. Niihara, Adv. Mater. 11 (1999) 1307.
[27] R. Kern, R. Sastrawan, J. Ferber, R. Stangl, J. Luther, Electrochim. Acta 47 (2002) 4213.
[28] A. Usami, Chem. Phys. Lett. 277 (1997) 105.
[29] D. Colonna, S. Colodrero, H. Lindström, A.D. Carlo, H. Míguez, Energy Environ. Sci. 5 (2012) 8238.
[30] W.G. Wang, H.Y. Zhang, R. Wang, M. Feng, Y.M. Chen, Nanoscale 6 (2014) 2390.
[31] P. Joshi, L.F. Zhang, D. Davoux, Z.T. Zhu, D. Galipeau, H. Fong, Q.Q. Qiao, Energy Environ. Sci. 3 (2010) 1507.
[32] J. Qian, P. Liu, Y. Xiao, Y. Jiang, Y. Cao, X. Ai, H. Yang, Adv. Mater. 21 (2009) 3663.
[33] Q. Wang, S. Ito, M. Grätzel, F. Fabregat-Santiago, I. Mora-Seró, J. Bisquert, T. Bessho, H. Imai, J. Phys. Chem. B 110 (2006) 25210.
[34] Q. Wang, J.E. Moser, M. Grätzel, J. Phys. Chem. B 109 (2005) 14945.
[35] R. Buonsanti, E. Carlino, C. Giannini, D. Altamura, L.D. Marco, R. Giannuzzi, M. Manca, G. Gigli, P.D. Cozzoli, J. Am. Chem. Soc. 133 (2011) 19216.
[36] W. Ho, J.C. Yu, J. Yu, Langmuir 21 (2005) 3486.
[37] J. Bisquert, F.F. Santiago, I.M. Seró, G.G. Belmonte, S. Gim'enez, J. Phys. Chem. C 113 (2009) 17278.
[38] P. Qiang, Z. Chen, P. Yang, X. Cai, S. Tan, P. Liu, W. Mai, Nanotechnology 24 (2013) 435403.
[39] K. Saravanan, K. Ananthanarayanan, P. Balaya, Energy Environ. Sci. 3 (2010) 939.